NANO EXPRESS

# Light-activated Multilevel Resistive Switching Storage in Pt/Cs$_2$AgBiBr$_6$/ITO/Glass Devices

Tingting Zhong, Yongfu Qin[†], Fengzhen Lv[*], Haijun Qin and Xuedong Tian

Abstract

High-density Cs$_2$AgBiBr$_6$ films with uniform grains were prepared by a simple one-step and low-temperature sol–gel method on indium tin oxide (ITO) substrates. An explicit tristate bipolar resistance switching behavior was observed in the Pt/Cs$_2$AgBiBr$_6$/ITO/glass devices under irradiation of 10 mW/cm^2 (445 nm). This behavior was stable over 1200 s. The maximum ratio of the high and low resistance states was about 500. Based on the analysis of electric properties, valence variation and absorption spectra, the resistive switching characteristics were attributed to the trap-controlled space charge-limited current mechanism due to the bromine vacancies in the Cs$_2$AgBiBr$_6$ layer. On the other hand, it is suggested that the ordering of the Schottky-like barrier located at Pt/Cs$_2$AgBiBr$_6$ affects the three-state resistance switching behavior under light irradiation. The ability to adjust the photoelectrical properties of Cs$_2$AgBiBr$_6$-based resistive switching memory devices is a promising strategy to develop high-density memory.

Keywords: Light regulation, Cs$_2$AgBiBr$_6$, Multilevel resistive switching, Bromine vacancy, Space charge-limited current mechanism, Schottky-like barrier

Graphical Abstract
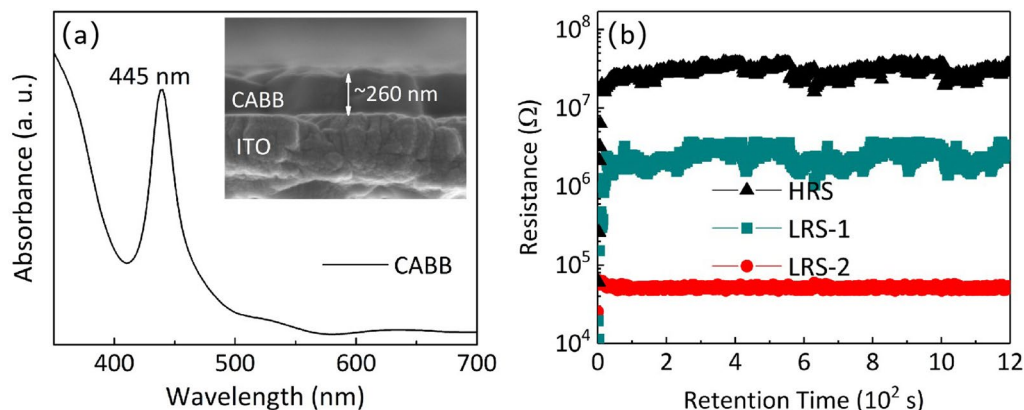
*Correspondence: lvfzh17@mailbox.gxnu.edu.cn
[†]Y. F. Qin: Equal contributor.
School of Physical Science and Technology and Guangxi Key Laboratory of Nuclear Physics and Technology, Guangxi Normal University, Yucai Road, Guilin 541000, China
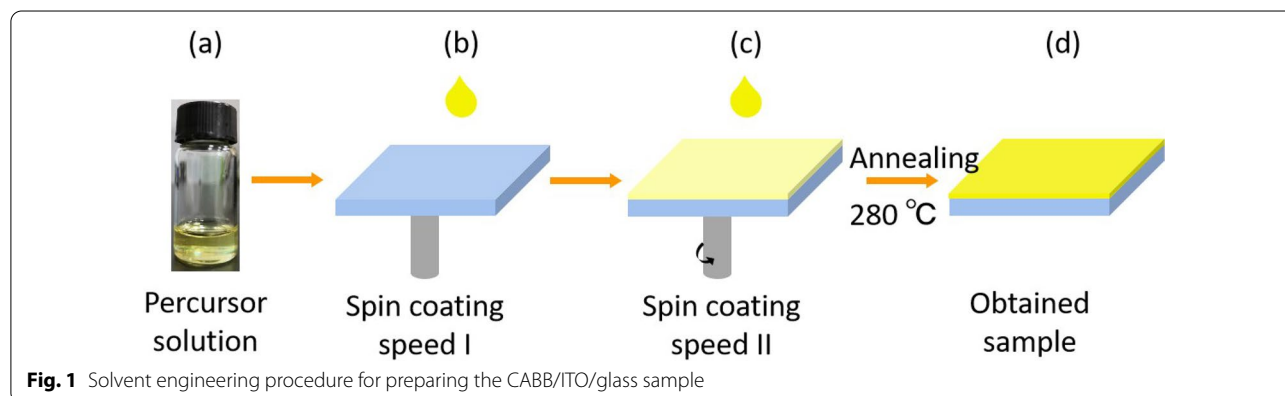
Introduction

With the increase of redundancy and complexity of information, demands for higher density, faster speed, smaller scale and lower consumption have brought about new

Zhong *et al. Nanoscale Research Letters* 2021, **16**(1):178

Page 2 of 9

development of new concept of information storage [1, 2]. The nonvolatile resistive random access memory (RRAM) is the most promising data storage candidate due to its simple structure, high write/read speed and low-scale limit and power consumption [2–4]. RRAM devices operated by a single electrical input have been widely researched and reported. However, this single input method faces the problem of the discovery of the appropriate media layer, the lowering of the power consumption and the problem of the multifunction expansion [5, 6]. Thus, the exploration of storage strategies that combine multiple physical channels, *e.g.*, optical, electric and magnetic fields, has been extensively undertaken [5–8]. Among them, the optical field is used as an extra terminal of a photoelectric materials-based RRAM device to ensure large memory windows and multiple storage levels greatly [5, 6, 9, 10]. Among various photoelectric materials, lead-based perovskites ($APbX_3$; with $A = Cs^+$, $CH_3NH_3^+$, $(H_2N)_2CH^+$, *etc.*) have been widely researched in photonic memristors due to their fast optical response, high photoelectric conversion efficiency and large defect tolerance [11–14]. However, the toxicity of soluble lead content and the long-term instability limit the broad application of $APbX_3$-based photoelectronic memories [15, 16]. Above hindrances have triggered the exploration of lead-free alternatives with higher stability. Recently, lead-free double perovskites have been proposed in the chemical formula $A_2M^+M^{3+}X_6$, where M^+ (monovalent cation) and M^{3+} (trivalent cation) are used to replace Pb^{2+} [17, 18]. Here, silver-bismuth double perovskites (e.g., $Cs_2AgBiBr_6$ and $Cs_2AgBiCl_6$) have extensively aroused concern due to the higher chemical stability, lower toxicity and more excellent optoelectronic property [15, 19, 20]. Although the potential for solar cells, photovoltaic devices and photoelectric detectors has been studied, photoelectric storage applications are not fully utilized [21–23].

In this study, high-density $Cs_2AgBiBr_6$ (CABB) films with high coverage were prepared by a simple one-step and low-temperature sol–gel method on indium tin oxide (ITO) substrates. Tristate RS characteristics, one high resistance state (HRS, i.e., OFF state) and two low resistance states (LRSs, i.e., ON states), were achieved in the Pt/CABB/ITO/glass devices under the light illumination (445 nm) of 10 mW/cm². The maximum resistance ratio between HRS and LRSs reached about 500. The current behavior was controlled by trap-controlled space charge-limited current (SCLC) mechanism owing to abundant bromine vacancies (V_{Brs}) in the CABB layer. Under light illumination, bias voltage sweep caused more V_{Brs} to be formed and captured/released electrons during the trapping/detrapping processes. In addition, the change of Pt/CABB Schottky-like barrier by the optical modulation also contributes to the multilevel RS behavior. This work demonstrates that CABB has the potential application in light-assisted multilevel storage devices. Related findings also provide an opportunity to understand the inherent nature of lead-free halide perovskites for their usage in high-density and nonvolatile optoelectronic memories.

Methods

Prior to the growth of the samples, the ITO/glass substrate was washed sequentially with acetone, isopropyl alcohol and deionized water and dried under a nitrogen gas flow. In the anhydrous dimethyl sulfoxide (DMSO, 1mL), 1.2 mmol of CsBr, 0.6 mmol of AgBr and 0.6 mmol of $BiBr_3$ were dissolved. The yellow precursor solution was obtained after stirring for 12 h at 65 °C in an Ar-filled glove box, as shown in Fig. 1a. The precursor solution was dripped onto an ITO/glass substrate and spin-coated at 500 rpm (speed I) for 15 sec and 5000 rpm (speed II) for 45 sec [Fig. 1b, c]. Finally, as shown in Fig. 1d, the yellowish film was obtained by annealing on a hot plate at 280 °C for 5 min.

Fig. 1 Solvent engineering procedure for preparing the CABB/ITO/glass sample

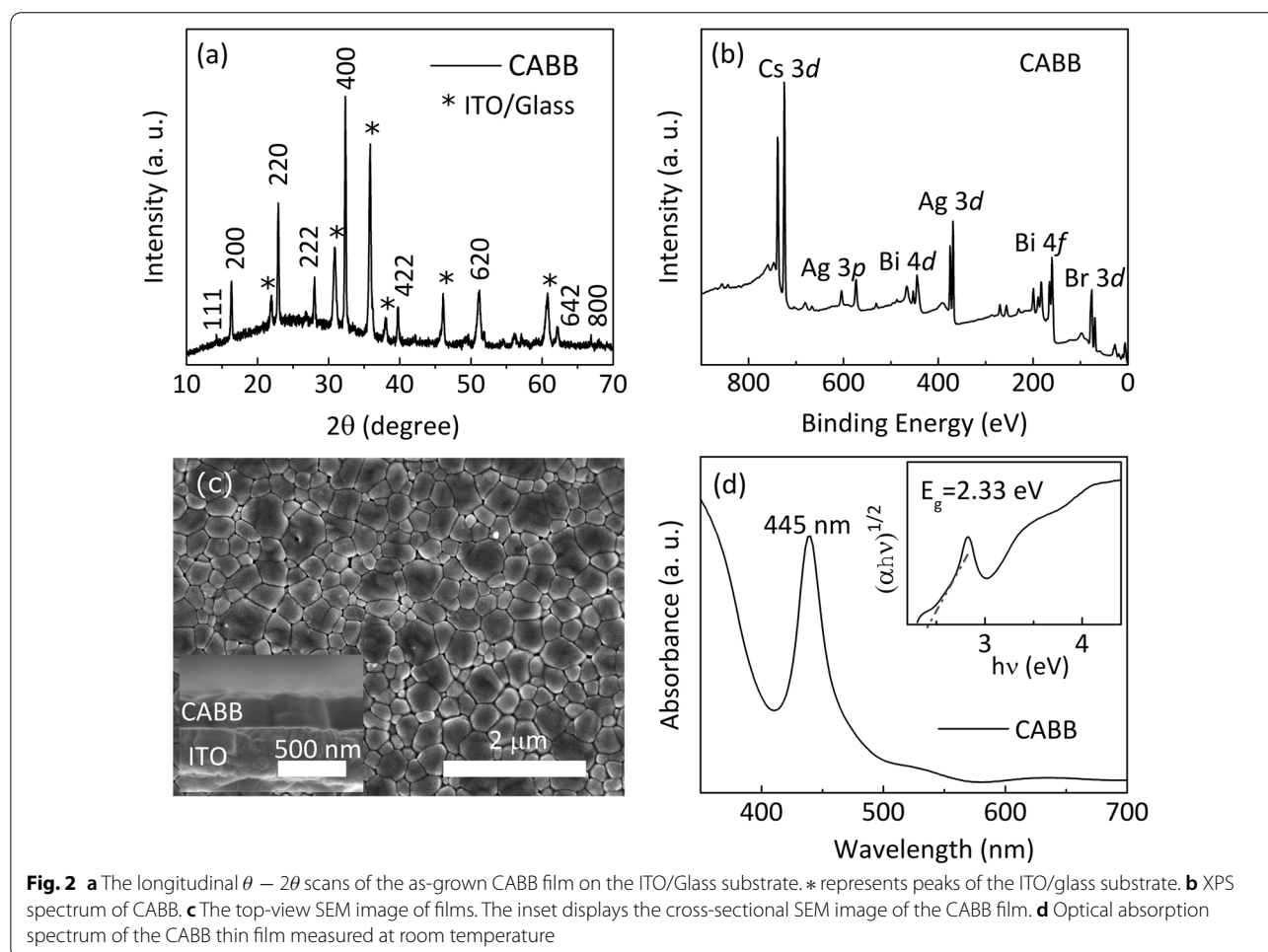Zhong *et al. Nanoscale Research Letters* 2021, **16**(1):178
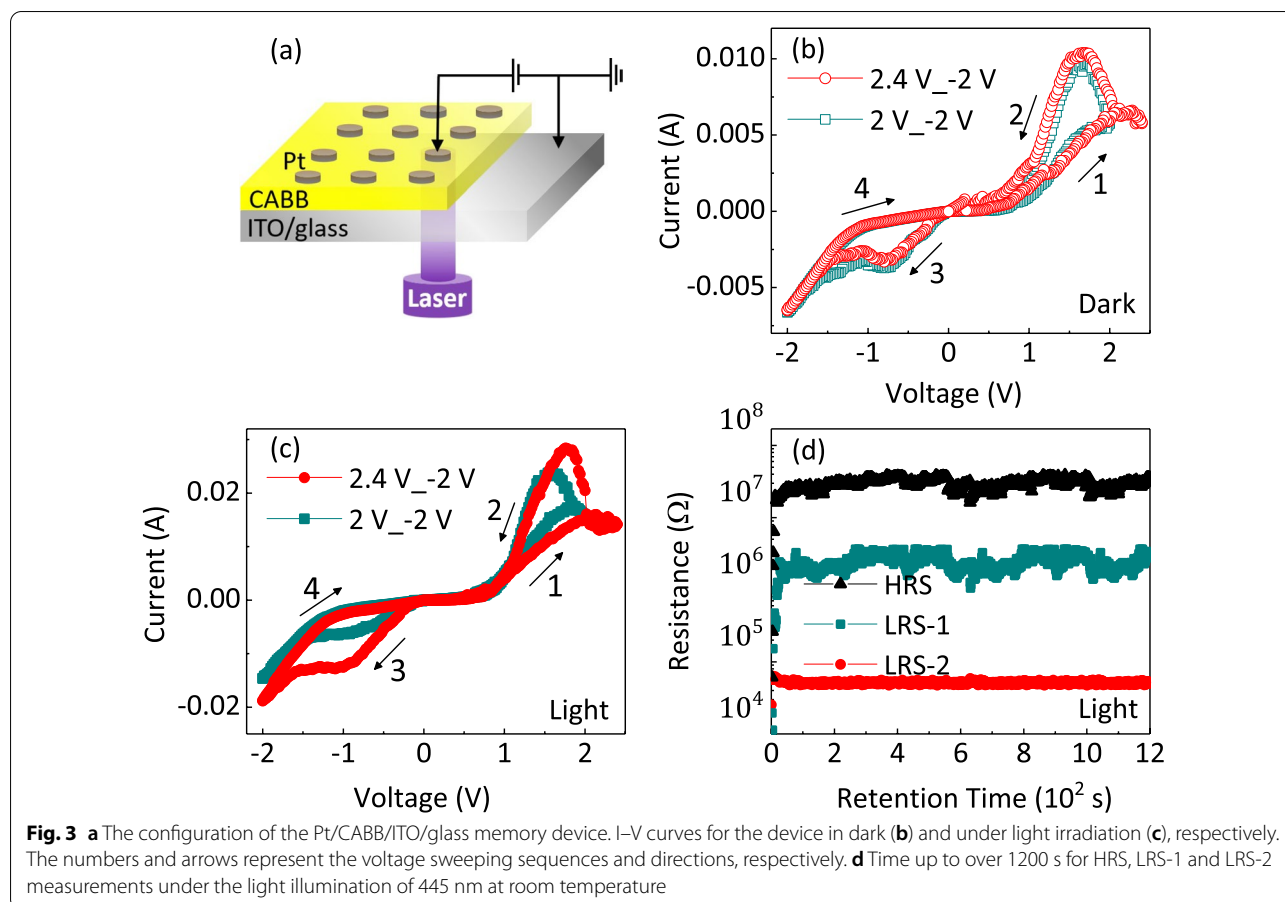
Page 3 of 9

Characterization

The crystallinity and phase purity of samples were investigated using X-ray diffraction (XRD, Mini-Flex600, Rigaku Corporation, Japan) with a Cu Kα radiation at room temperature. The compositional analysis and band structure of Pt/CABB/ITO cells were performed by X-ray photoelectron spectroscopy (XPS) and Ultraviolet photoelectron spectroscopy (UPS) with a monochromatic Al K$_\alpha$ X-ray source, respectively (XPS/UPS, ESCALAB250Xi, Thermo Fisher Scientific, America). A UV–Vis reflectance spectrum was recorded using a UV-2700 spectrophotometer (Shimadzu Corporation, Japan). Microscope images of the CABB film morphologies were recorded by a field-emission scanning electron microscope (SEM, FEI Quanta 200, FEI, Holland). All current–voltage (*I–V*) characteristics of the cells in Pt/CABB/ITO/glass configuration were examined using a Keithley 2400 SourceMeter.

Results and Discussion

Figure 2a exhibits that the XRD peaks are distributed in the (111), (200), (220), (222), (400), (422), (620) and (642) planes of crystalline CABB, corresponding to the cubic phase of CABB [24–26]. The wide spectrum of XPS clearly presents only Cs, Ag, Bi and Br elements in the samples, indicating that the chemical composition of the CABB film is pure [Fig. 2b]. The top view of the surface morphology reveals that CABB films possess a high surface coverage and relatively uniform crystal grains. Many obvious grain boundaries provide channels to the migration of ions and vacancies. And these grain boundaries can promote a further reduction in conductive energy barriers of ions and vacancies due to their light sensitivity [27, 28]. The CABB layer which has a uniform thickness of ~260 nm is clearly visible in the inset of Fig. 2c. UV–Vis absorption spectrum indicates that an excitonic absorption band in the region from 420 to 500 nm, the peak locates at 445 nm [Fig. 2d].

Figure 3a displays the schematic structure of the fabricated CABB-based device under violet light (445 nm) of

Fig. 2 **a** The longitudinal $\theta - 2\theta$ scans of the as-grown CABB film on the ITO/Glass substrate. * represents peaks of the ITO/glass substrate. **b** XPS spectrum of CABB. **c** The top-view SEM image of films. The inset displays the cross-sectional SEM image of the CABB film. **d** Optical absorption spectrum of the CABB thin film measured at room temperature

Zhong *et al. Nanoscale Research Letters* 2021, **16**(1):178

Page 4 of 9

Fig. 3 a The configuration of the Pt/CABB/ITO/glass memory device. I–V curves for the device in dark (**b**) and under light irradiation (**c**), respectively. The numbers and arrows represent the voltage sweeping sequences and directions, respectively. **d** Time up to over 1200 s for HRS, LRS-1 and LRS-2 measurements under the light illumination of 445 nm at room temperature

10 mW/cm^2, where a CABB layer is sandwiched between the Pt-based top electrode (TE) and the ITO-based bottom electrode (BE). The bias voltage is applied on the Pt TE of the device, while the ITO BE is grounded. As exhibited in Fig. 3b, by applying voltage loops to the Pt/CABB/ITO/glass device with a periodic sweeping (0 V→2 V/2.4 V→-2 V→0 V), an obvious current hysteresis is observed during the voltage sweeping in the dark condition. The device presents a typical bipolar RS behavior. However, different resistance states are not observed under different operating voltages. When the device was exposed in the light with a laser of 445 nm, 10 mW/cm^2, the current distinctly switched between two correspondingly different LRSs in the negative region, as shown in Fig. 3c. The device presents obvious tristate RS behavior under the light illumination. Three different resistance states, HRS, LRS-1 and LRS-2, were recorded at a low reading voltage ($V_r = -0.1$ V) under light illumination. As illustrated in Fig. 3d, the maximum resistance ratio of HRS and LRSs is about 500 at V_r. HRS, LRS-1 and LRS-2 can be stably maintained and no obvious degradation occurs after 1200 s. The above results illustrate that Pt/CABB/ITO/glass devices possess the fine retention ability and

the multilevel storage potential. In order to confirm the optimal condition of light-activated multilevel RS characteristics, we measured the RS behavior of Pt/CABB/glass devices under different light intensities (Additional file 1: Fig. S1). Compared with the *I–V* curve measured under the light intensity of 10 mW/cm^2 [Fig. 3d], different LRSs could not be obviously observed in the negative bias voltage region under the light intensities of 8 mW/cm^2 and 13 mW/cm^2, as shown in Additional file 1: Fig. S1a, b. Moreover, as the light intensity increases, although the multilevel RS characteristics appear, the maximum ratio of HRS and LRSs under the intensities of 8 mW/cm^2 is 13 mW/cm^2 are just ~10 and ~3, respectively [Additional file 1: Fig. S1c, d]. And the stability of multilevel RS characteristics under these intensities is not good as that of 10 mW/cm^2. Aiming at the influence and law of different light intensities for the RS behavior of CABB-based memories will be researched and discussed in our next work.

The bipolar RS behavior in different memories can be normally explained by three types of mechanisms, namely the electrochemical metallization mechanism (ECM), the valence variation mechanism (VCM) and the

Zhong *et al. Nanoscale Research Letters* 2021, **16**(1):178

Page 5 of 9

thermochemical mechanism (TCM) [12, 29]. In the ECM model, the RS switching behavior is based on the formation or rupture of metallic conductive filaments formed by active metal atoms within the medium layer [12, 30]. However, the inert Pt metal was applied to be as the electrode of the CABB-based memory device in our work; thus, we speculated that the VCM model was primarily contributed to the RS behavior in the Pt/CABB/ITO/glass device. As illustrated in Fig. 4, the I–V curve is replotted on double logarithmic coordinates in the positive and negative voltage sweep regions. In the positive region, the fitting slope of log(I)–log(V) curve is approximately 1 in the voltage range of 0 and 0.3 V, the I–V relationship obeys the Ohm's law. With the positive voltage increasing, the slopes of the fitted lines are approximately 2 and 10 in the voltage range of 0.3 V and 1.1 V, respectively, indicating that the SCLC model dominates the conductive process [12, 30, 31]. With the positive bias further increasing in the range of 1.1 V and 1.9 V, the current decreases obviously, indicating the so-called negative differential resistance (NDR) appearing [32]. When the positive bias reaches V_{SET} (+2 V), the device switches from HRS to LRS, and then, the relationship of log(I)–log(V) obeys $I \propto V^2$ (1.8 V–0.2 V). Subsequently, a linear relation is quickly observed between I and V. The conductive behavior obeys Ohmic conduction even though the bias reversely sweeps. When the device switches from LRS to HRS under V_{RESET} (−2 V), the slope of the fitted curve recovers about 8 and 2 in the range of −2 V and −0.5 V, respectively, suggesting that the SCLC mechanism dominates this HRS region. With the negative voltage decreasing further, the I–V follows the Ohmic conduction.

To trace and confirm the origin of SCLC conductive mechanism in the Pt/CABB/I TO/ glass device, XPS measurement was taken to investigate the valence variation of the fabricated CABB films. As shown in Fig. 5a,
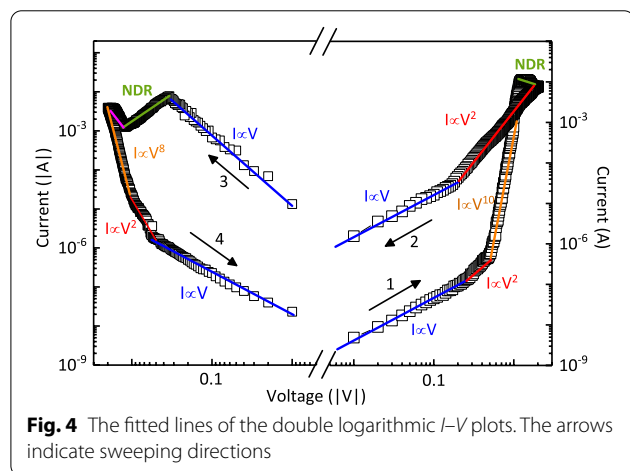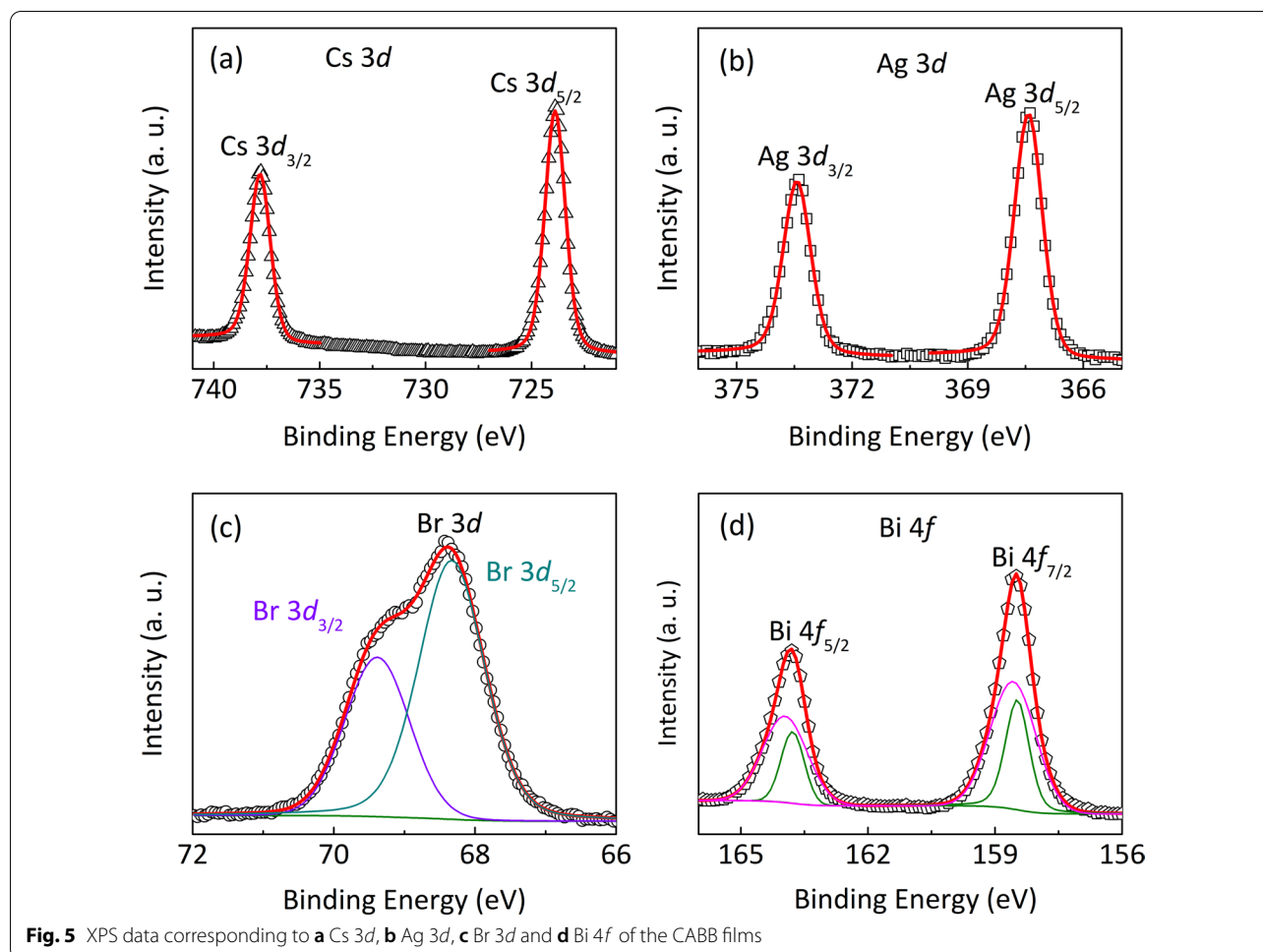
two clear peaks at 737.83 eV and 723.88 eV are observed corresponding to Cs^+ [33]. The presence of Ag^+ is also revealed according to the peaks located at 373.43 eV and 367.42 eV ascribed to $3d_{3/2}$ and $3d_{5/2}$, respectively [Fig. 5b]. The fitting results of Cs and Ag elements are consistent with the valence composition in the CABB films. As depicted in Fig. 5c, the doublet peaks of Br $3d_{3/2}$ and Br $3d_{5/2}$ signals locate at 69.38 eV and 68.33 eV, respectively. Obviously, they shift toward the positive positions, indicating that V_{Brs} generate in the CABB layer [34]. In addition, as illustrated in Fig. 5d. Bi $4f_{5/2}$ and Bi $4f_{7/2}$ regions are fitted into two peaks, respectively. The main peaks at 163.96 eV and 158.60 eV are assigned to Bi^{3+}, and two peaks with lower binding energy at 163.78 eV and 158.48 eV are ascribed to the low valence state $Bi^{(3-x)+}$, indicating the generation of V_{Brs} in the CABB layer [35].
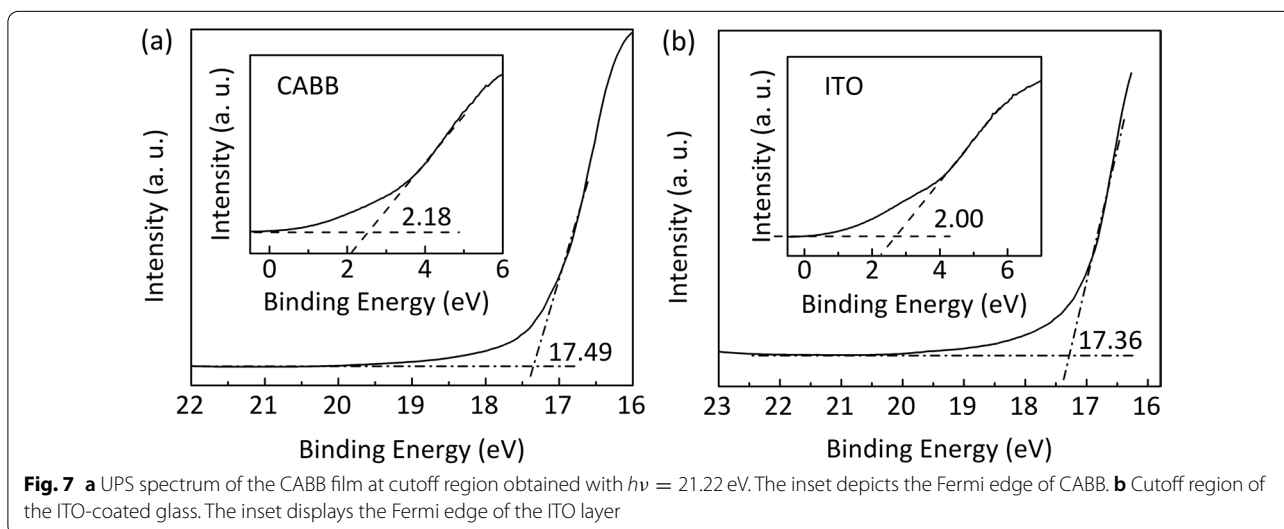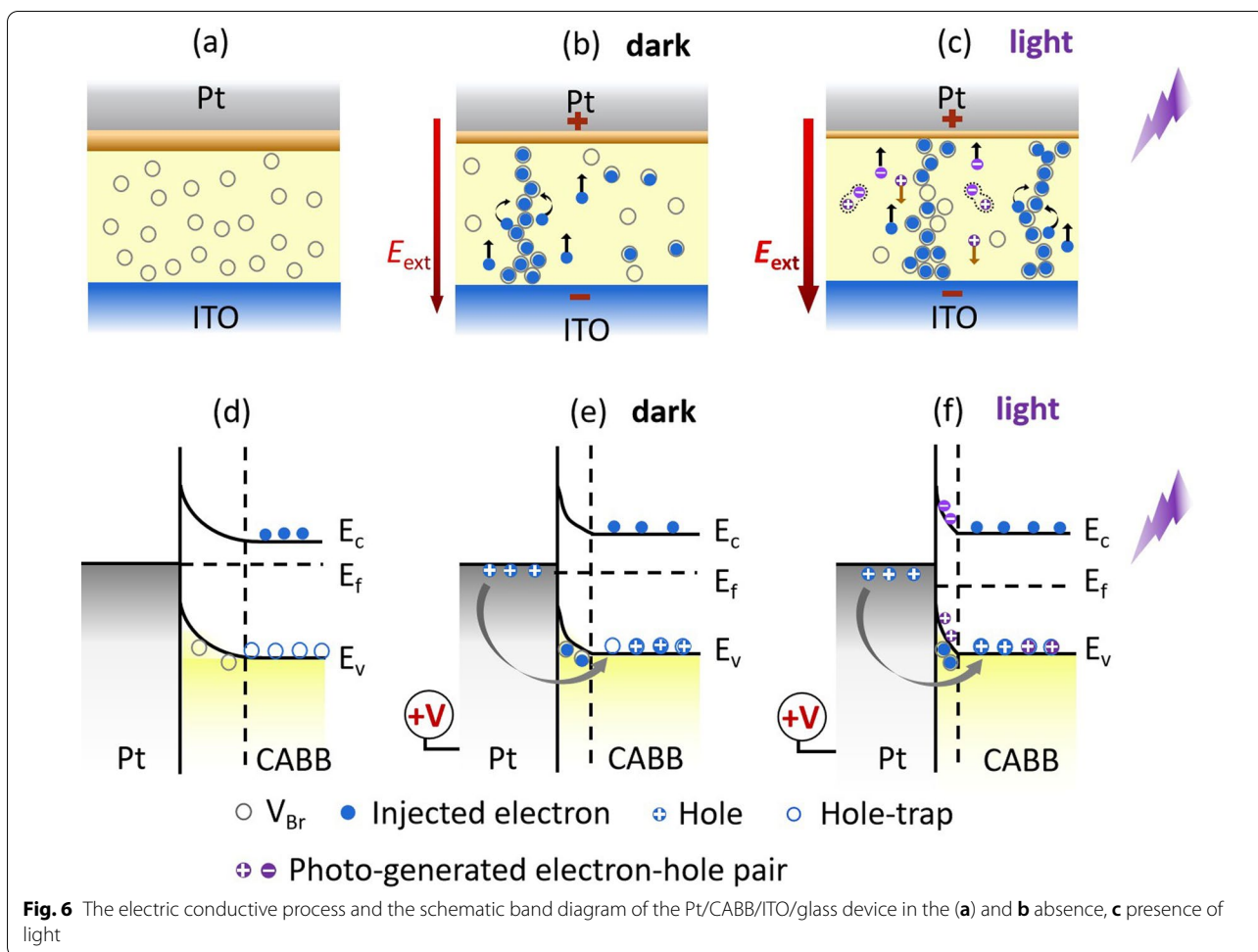
Initially, the Pt/CABB/ITO/glass device is difficult to conduct electricity and stays in the HRS due to V_{Brs} randomly disperse in the CABB layer [Fig. 6a]. When a low positive bias is applied to the Pt TE, an external electric field (E_{ext}) is formed in the CABB layer, which points from Pt TE to ITO BE. The I–V relationship follows Ohm's law own to the conduction of thermally excited electrons in the CABB layer. With the E_{ext} increasing, the electrons injected from the ITO BE are captured by V_{Brs} in the CABB layer, the relationship of I–V follows Child's low ($I \propto V^2$), as shown in Fig. 6b. With E_{ext} increasing further, the Br^- ions are attracted to the Pt TE, creating more V_{Brs} to capture electrons during the trapping process. When the positive bias arrives V_{SET}, V_{Brs} form conduction channels due to the lowest activation energy; the injected electrons can migrate by vacancy to vacancy hopping [9, 36]. The device switches from HRS to LRS and remains Ohmic conduction even though the bias sweeps reversely. While the Pt/CABB/ITO device is exposed under the light irradiation of 445 nm, photoinduced electron–hole pairs generate in the CABB layer [Fig. 6c]. With the E_{ext} increasing, electron–hole pairs are divided. Photo-generated holes can recombine with Br^-, promoting the generation of V_{Brs} in the CABB film [37]. In the meantime, the driving force (zeE) that drives the migration of V_{Brs} is enhanced, causing the activation energy of V_{Brs} lowering by [$-\varepsilon/2$ ($\varepsilon \propto zeE$)]; more V_{Brs} generate in the CABB film [27, 38]. Thus, more conductive paths composed of V_{Brs} form and participate in the RS process under bias voltage sweeping. When an opposite voltage is applied to the Pt TE and goes across V_{RESET}, the trapped electrons are drawn out from V_{Brs}, and the current behavior obeys the SCL conduction. The relationship of I–V follows $I \propto V^2$. Meanwhile, the bridges of V_{Brs} are ruptured resulting from the reverse migration of Br^- ions influenced by the negative voltage. And thus,

Fig. 4 The fitted lines of the double logarithmic I–V plots. The arrows indicate sweeping directions

Zhong *et al. Nanoscale Research Letters* 2021, **16**(1):178

Page 6 of 9

Fig. 5 XPS data corresponding to **a** Cs 3*d*, **b** Ag 3*d*, **c** Br 3*d* and **d** Bi 4*f* of the CABB films

the device switches from LRS to HRS. The above evolution of Br$^-$ conductive channels has been measured and researched by the conducting atomic force microscopy in our previous work [26]: When a positive bias voltage was applied to the CABB film, obvious current channels were observed, indicating that the conductive filaments were formed in the CABB layer; when a negative bias voltage was applied to scan the same area, the layer could not present obvious current, suggesting that the conductive filaments were ruptured under the negative voltage.

Moreover, the change of barrier located at the interface of electrodes and RS functional layers is also contributed to the RS behavior under light irradiation [39, 40]. Figure 7a, b shows the Fermi and cutoff regions of CABB and ITO in the UPS spectra, respectively. The work function of the CABB film and the ITO BE is calculated as 5.91 eV and 5.86 eV, respectively. Thus, the contact type between ITO and CABB is Ohmic. The Schottky-like barrier generates in the Pt/CABB interface due to the larger work function of Pt (6.42 eV) [41]. Figure 6d shows the initial schematic band diagram of the Pt/CABB junction in the

dark condition. The energy band of the CABB layer bends upward and a Schottky-like barrier forms in the Pt/CABB interface due to the higher Fermi level (E$_f$) of CABB. The barrier prevents electrons transferring across the Pt/CABB interface, and the Pt/CABB/ITO/glass device remains in HRS. When the positive V_{SET} applied to the Pt TE, V$_{Brs}$ gradually are filled by electrons injected from the ITO BE in the depletion region near the Pt/CABB interface. The width and height of the Schottky-like barrier is lowered [Fig. 6e]. In the meantime, the holes can inject from the Pt electrode across the Pt/CABB interface and fill the hole traps distributed near the valence band (VB) of CABB [39]. With the hole concentration increasing at the Pt/CABB interface, the E$_f$ of CABB moves toward to the VB, causing the barrier further lowering. And thus, the Pt/CABB/ITO/glass device switches from HRS to LRS. When the device is exposed to light illumination with a wavelength of 445 nm ($\sim$2.79 eV), plenty of photoinduced electron–hole pairs generate in the CABB layer, and then, they are separated by the E_{ext}. Photogenerated electrons jump into the conduction band (CB)

Zhong *et al. Nanoscale Research Letters* 2021, **16**(1):178

Page 7 of 9

Fig. 6 The electric conductive process and the schematic band diagram of the Pt/CABB/ITO/glass device in the (**a**) and **b** absence, **c** presence of light

Fig. 7 a UPS spectrum of the CABB film at cutoff region obtained with $h\nu = 21.22$ eV. The inset depicts the Fermi edge of CABB. **b** Cutoff region of the ITO-coated glass. The inset displays the Fermi edge of the ITO layer

Zhong *et al. Nanoscale Research Letters* 2021, **16**(1):178

Page 8 of 9

and become free electrons because they obtain enough energy; photo-generated holes intensify the band bending and constantly facilitate electron transport across the junction with a thinner Schottky-like barrier, as shown in Fig. 6f. In the meantime, the hole traps can capture photo-generated holes, causing the E_f shifts toward VB and leaving a lower Schottky-like barrier. In addition, more holes inject from Pt electrode can also be trapped by the hole traps [39]. Hence, the height of barrier further decreases. Continuous illumination hinders the recombination of electron–hole pairs and further reduces the inhibiting effect of the barrier, so the devices remain in LRS. Under the negative V_{RESET}, V_{Brs} move toward the Pt/CABB interface, the barrier recovers its original height and width, and the device switches back to its original HRS.

Conclusions

In summary, light-assisted tristate bipolar RS characteristics were observed in the Pt/CABB/ITO/glass memory devices. The maximum ON/OFF ratio was ~500, and different resistance states could be steadily maintained over 1200 s. The RS behavior was principally attributed to the trap-controlled SCLC mechanism, and charge traps composed of V_{Brs} were considered to play a key role in forming the conductive paths. The modulation of the Pt/CABB Schottky-like barrier under light illumination was also responsible for the RS behavior of the devices in the carrier injection-trapped/detrapped process. These results illustrate the potential multilevel storage capacity of the lead-free double perovskites in the optoelectronic memory field.

Abbreviations

RRAM: Resistive switching random access memory; CABB: $Cs_2AgBiBr_6$; ITO: Indium tin oxide; RS: Resistive switching; TE: Top electrode; BE: Bottom electrode; ECM: Electrochemical metallization mechanism; VCM: Valence variation mechanism; TCM: Thermochemical mechanism; *I–V*: Current–voltage; SCLC: Space charge-limited current; LRS: Low resistance states; HRS: High resistance state; V_{SET}: Set voltage; V_{RESET}: Reset voltage; V_r: Read voltage; V_{Brs}: Bromine vacancies; CB: Conduction band; VB: Valence band; E_f: Fermi level; E_{ext}: External electric field; XRD: X-ray diffractometry; XPS: X-ray photoelectron spectroscopy; UPS: Ultraviolet photoelectron spectroscopy; SEM: Scanning electron microscopy.

Supplementary Information

The online version contains supplementary material available at https://doi.org/10.1186/s11671-021-03636-6.

Additional file 1. Supplementary Information.

Acknowledgements

Authors' Contributions
Tingting Zhong made substantial contribution to preparation of samples, acquisition of data, analysis and interpretation of data and drafting the article. Yongfu Qin made contribution to preparation of samples and analysis and interpretation of data. Fengzhen Lv made contribution to conception and design, analysis and interpretation of data, funding acquisition, writing-review. Haijun Qin made contribution to analysis and interpretation of data. Xuedong Tian provided the funding support. All authors read and approved the final manuscript.

Availability of Data and Materials
All data generated and analyzed during this study are included in this article and the attached supporting information.

Declarations

Competing interests
The authors declare that they have no competing interests.

References

1. Waser R, Aono M (2007) Nanoionics-based resistive switching memories. Nat Mater 6:833–843
2. Zahoor F, Zulkifli TZA, Khanday FA (2020) Resistive random access memory (RRAM): an overview of materials, switching mechanism, performance, multilevel cell (mlc) storage, modeling, and applications. Nanoscale Res Lett 15(90)
3. Wang H, Meng FB, Cai YR, Zheng LY, Li YG, Liu YJ, Jiang YY, Wang XT, Chen XD (2013) Resistive switching phenomena in thin films: materials, devices, and applications. Adv Mater 25:108–114
4. Ding XX, Feng YL, Huang P, Liu LF, Kang JF (2019) Low-power resistive switching characteristic in HfO_2/TiO_x Bi-layer resistive random-access memory. Nanoscale Res Lett 14(157)
5. Ye CQ, Peng Q, Li MZ, Luo J, Tang ZM, Pei J (2012) Multilevel conductance switching of memory device through photoelectric effect. J Am Chem Soc 134:20053–20059
6. Mao JY, Zhou L, Zhu XJ, Zhou Y, Han S (2019) Photonic memristor for future computing: a perspective. Adv Opt Mater 1900766:1–15
7. Prezioso M, Riminucci A, Graziosi P, Bergenti I, Rakshit R, Cecchini R, Vianelli A, Borgatti F, Haag N, Willis M, Drew AJ, Gillin WP, Dediu VA (2013) A single-device universal logic gate based on a magnetically enhanced memristor. Adv Mater 25:534–538
8. Liu SS, Jin C, Zheng DX, Pang X, Wang YC, Wang P, Zheng WC, Bai HL (2019) Ferroelectric field manipulated nonvolatile resistance switching in $Al:ZnO/Pb(Mg_{1/3}Nb_{2/3})_{0.7}Ti_{0.3}O_3$ heterostructures at room temperature. Phys Chem Chem Phys 21:10784–10790
9. Wang SK, Sun XW, Li GH, Jia CH, Li GQ, Zhang WF (2018) Study on the multi-level resistance-switching memory and memory-state-dependent photovoltage in $Pt/Nd: SrTiO_3$ junctions. Nanoscale Res Lett 18
10. Russo P, Xiao M, Liang R, Zhou NY (2018) UV-induced multilevel current amplification memory effect in zinc oxide rods resistive switching devices. Adv Funct Mater 706230:1–9
11. Choi J, Han JS, Jang HW (2018) Organic-inorganic hybrid halide perovskites for memories, transistors, and artificial synapses. Adv Mater 1704002:1–21
12. Gao S, Yi XL, Shang J, Liu G, Li RW (2019) Organic and hybrid resistive switching materials and devices. Chem Soc Rev 48:1531–1565
13. Kim HJ, Han JS, Kim SG, Kim SY, Jang HW (2019) Halide perovskites for resistive random-access memories. J Mater Chem C 7:5226–5234

Zhong *et al. Nanoscale Research Letters*   2021, **16**(1):178

Page 9 of 9

14. Lv FZ, Ling K, Zhong TT, Liu FC, Liang XG, Zhu CM, Liu J, Kong WJ (2020) Multilevel resistive switching memory based on a $CH_3NH_3PbI_{3-x}Cl_3$ film with potassium chloride additives. Nanoscale Res Lett 15:126

15. Cheng XF, Qian WH, Wang J, Yu C, He J, Li H, Xu Q, Chen D, Li NJ, Lu JM (2019) Environmentally robust memristor enabled by lead-free double perovskite for high-performance information storage. Small 1905731:183–210

16. Ke WJ, Kanatzidis WG (2019) Prospects for low-toxicity lead-free perovskite solar cells. Nat Commun 10:1–4

17. Chu L, Ahmad W, Liu W, Yang J, Zhang R, Sun Y, Yang JP, Li XA (2019) Lead-free halide double perovskite materials: a new superstar toward green and stable optoelectronic applications. Nano-Micro Lett 11:1–18

18. Zhao XG, Yang DW, Ren JC, Sun YH, Xiao ZW, Zhang YZ (2018) Rational design of halide double perovskites for optoelectronic applications. Joule 2:1662–1673

19. Kamat PV, Bisquert J, Buriak J (2017) Lead-free perovskite solar cells. ACS Energy Lett 2:904–905

20. Lee DE, Kim SY, Jang HW (2020) Lead-free all inorganic halide perovskite quantum dots: review and outlook. J Eur Ceram Soc 57:455–479

21. Longo G, Mahesh S, Buizza LRV, Wright AD, Ramadan A, Abdi-Jalebi M, Nayak PK, Herz LM, Snaith HJ (2020) Understanding the performance limiting factors of $Cs_2AgBiBr_6$ double-perovskite solar cells. ACS Energy Lett 5:2200

22. Greul E, Petrus ML, Bineka A, Docampob P, Being T (2017) Highly stable, phase pure $Cs_2AgBiBr_6$ double perovskite thin films for optoelectronic applications. J Mater Chem A 5:1997–19981

23. Pan WC, Wu HD, Luo JJ, Deng ZZ, Ge C, Chen C, Jiang XW, Yin WJ, Niu GD, Zhu L, Yin LX, Zhou Y, Xie QG, Ke XX, Sui ML, Tang J (2017) $Cs_2AgBiBr_6$ single-crystal x-ray detectors with a low detection limit. Nat Photonics 11:726–732

24. Lei LZ, Shi ZF, Li Y, Ma YY, Zhang F, Xu TT, Tian YT, Wu D, Lia WJ, Du GT (2018) High-efficiency and air-stable photodetectors based on lead-free double perovskite $Cs_2AgBiBr_6$ thin films. J Mater Chem C 00:1–3

25. Ning WH, Wang F, Wu B, Yan Z, Liu XJ, Tao YT, Liu JM, Huang W, Fahlman M, Hultman L, Sum T, Gao F (2018) Long electron-hole diffusion length in high-quality lead-free double perovskite films. Adv Mater 30:1706246

26. Lv FZ, Zhong TT, Qin YF, Qin HJ, Wang WF, Liu FC, Kong WJ (2021) Resistive switching characteristics improved by visible-light irradiation in a $Cs_2AgBiBr_6$-based memory device. Nanomaterials 11:1361

27. Ham S, Choi S, Cho H, Na SI, Wang G (2019) Photonic organolead halide perovskite artificial synapse capable of accelerated learning at low power inspired by dopamine-facilitated synaptic activity. Adv Funct Mater 29:1806646

28. Yuan YB, Huang JS (2016) Ion migration in organometal trihalide perovskite and its impact on photovoltaic efficiency and stability. Acc Chem Res 49:286–293

29. Guo F, Zhao MT, Xu K, Huan Y, Ge SP, Chen YM, Huang JH, Cui YM, Zhuang JC, Du Y, Feng HF, Hao WC (2019) Evidence for dynamic relaxation behavior of oxygen vacancy in Aurivillius Bi_2MoO_6 from dielectric spectroscopy during resistance switching. J Mater Chem C 7:8915–8922

30. Chen ZL, Yu Y, Jin LF, Li YF, Li QY, Li TT, Li J, Zhao HL, Zhang YT, Dai HT, Yao JQ (2020) Broadband photoelectric tunable quantum dot based resistive random access memory. J Mater Chem C 8:2178–2185

31. Lv FZ, Ling K, Wang WF, Chen P, Liu FC, Kong WJ, Zhu CM, Liu J, Long LZ (2019) Multilevel resistance switching behavior in $PbTiO_3/Nb:SrTiO_3(100)$ heterostructure films grown by hydrothermal-epitaxy. J Alloy Compound 778:768–773

32. Chen J, Reed MA, Rawlett AM, Tour JM (1999) Large on-off ratios and negative differential resistance in a molecular electronic device. Science 286:1550–1552

33. Espejo GG, Padón DR, Luque R, Camacho L, Miguel G (2019) Mechanochemical synthesis of three double perovskite: $Cs_2AgBiBr_6$, $(CH_3NH_3)_2TlBiBr_6$ and $Cs_2AgSbBr_6$. Nanoscale 11:16650–16657

34. Zhu YY, Cheng PW, Shi J, Wang HJ, Liu Y, Xiong R, Ma HY, Ma HX (2019) Bromine vacancy redistribution and metallic-ion migration-induced air-stable resistive switching behavior in all-inorganic perovskite $CsPbBr_3$ film-based memory device. Adv Electron Mater 6:1900754

35. Zhang GQ, Cai L, Zhang YF, Wei Y (2018) Bi^{5+}, $Bi^{(3-x)+}$, and oxygen vacancy induced $BiOCl_xI_{1-x}$ solid solution toward promoting visible-light driven photocatalytic activity. Chem Eur J 24:7434–7444

36. Gu C, Lee JS (2016) Flexible hybrid organic-inorganic perovskite memory. ACS Nano 5:5413–5418

37. Cai HZ, Lao MM, Xu J, Chen YK, Zhong CJ, Lu SR, Hao A, Chen RQ (2019) All-inorganic perovskite Cs_4PbBr_6 thin films in optoelectronic resistive switching memory devices with a logic application. Ceram Int 45:5724–5730

38. Azpiroz JM, Mosconi E, Bisquertcd J, Angelis FD (2015) Defect migration in methylammonium lead iodide and its role in perovskite solar cell operation. Energy Environ Sci 8:2118

39. Zhou FC, Liu YC, Shen XP, Wang MY, Yuan F, Chai Y (2018) Low-voltage, optoelectronic $CH_3NH_3PbI_{3-x}Cl_x$ memory with integrated sensing and logic operations. Adv Funct Mater 28:1800080

40. Zheng PP, Sun B, Chen YZ, Elshekh H, Yu T, Mao SS, Zhu SH, Wang HY, Zhao Y, Yu Z (2019) Photo-induced negative differential resistance in a resistive switching memory device based on $BiFeO_3/ZnO$ heterojunctions. Appl Mater Today 14:21–28

41. Derry GN, Zhong ZJ (1989) Work function of Pt(111). Phys Rev B 39:39–40

Publisher's Note